





Double magnetic transitions and exotic field-induced phase in the triangular lattice antiferromagnets $\text{Sr}_3\text{Co}(\text{Nb},\text{Ta})_2\text{O}_9$

Surender Lal ¹, Sebin J. Sebastian ¹, S. S. Islam ¹, M. P. Saravanan,² M. Uhlarz,³ Y. Skourski,³ and R. Nath ^{1,*}

¹*School of Physics, Indian Institute of Science Education and Research, Thiruvananthapuram 695551, India*

²*Low Temperature Laboratory, UGC-DAE Consortium for Scientific Research, University Campus, Khandwa Road, Indore 452001, India*

³*Dresden High Magnetic Field Laboratory (HLD-EMFL), Helmholtz-Zentrum Dresden-Rossendorf, 01328 Dresden, Germany*



(Received 15 December 2022; revised 17 May 2023; accepted 13 July 2023; published 25 July 2023)

Two triangular lattice antiferromagnets $\text{Sr}_3\text{Co}(\text{Nb}, \text{Ta})_2\text{O}_9$ with an effective $j_{\text{eff}} = 1/2$ of Co^{2+} are synthesized and their magnetic properties are investigated via magnetization and heat capacity measurements. The leading in-plane antiferromagnetic exchange coupling is estimated to be $J/k_B \simeq 4.7$ and 5.8 K, respectively. Both compounds feature two-step magnetic transitions at low temperatures [$T_{N1} \simeq 1.47$ K and $T_{N2} \simeq 1.22$ K) and ($T_{N1} \simeq 0.88$ K and $T_{N2} \simeq 0.67$ K), respectively], driven by weak easy-axis anisotropy. Under magnetic field, $\text{Sr}_3\text{CoNb}_2\text{O}_9$ evinces a plateau at $1/3$ magnetization. Interestingly, the high-field magnetization of $\text{Sr}_3\text{CoTa}_2\text{O}_9$ reveals an exotic regime (between H_{S1} and H_{S2}) below the fully polarized state in which the heat capacity at low temperatures is governed by a power law ($C_p \propto T^\alpha$) with a reduced exponent $\alpha \simeq 2$. These results demonstrate an unusual field-induced state with gapless excitations in the strongly frustrated magnet $\text{Sr}_3\text{CoTa}_2\text{O}_9$. The complete T - H phase diagram is discussed for both compounds.

DOI: [10.1103/PhysRevB.108.014429](https://doi.org/10.1103/PhysRevB.108.014429)

I. INTRODUCTION

Geometrically frustrated magnets have attracted a revived interest because the frustration effect may cause the absence of magnetic long-range-order (LRO), leading to an abundance of novel states of matter [1,2]. The size of a local magnetic moment is also a convenient tuning parameter that controls the magnitude of quantum fluctuations and has broad implications on the ground state properties. For instance, a reduced spin value, especially spin-1/2, amplifies the effect of quantum fluctuations and precipitates more nontrivial ground states. A renowned testimony of magnetic frustration and quantum fluctuations is the quantum spin-liquid (QSL), a highly entangled and dynamically disordered many-body state [3]. Over the years, relentless efforts have been made to experimentally devise appropriate model compounds with spin-1/2 that may promote this disordered state.

A frustrated spin-1/2 triangular lattice antiferromagnet (TLAF) is widely believed to be a model system to host QSL driven by ground state degeneracy in two dimensions (2D) [4]. In an isotropic Heisenberg TLAF with only nearest-neighbor (NN) interaction, the spins order antiferromagnetically forming a 120° spin structure in zero magnetic field, known as a three-sublattice Néel state [5–7]. When an external magnetic field is applied, the Néel order is subverted and an “up-up-down” (*uud*) configuration is stabilized over a wide field range before reaching saturation. This results in a magnetization plateau at $1/3$ of the magnetic saturation stemming from quantum and/or thermal fluctuations [8,9]. Magnetic anisotropy and interactions beyond nearest-neighbor are also

two crucial parameters, inherently present in majority of the experimental systems, influence the ground state significantly, and give rise to more complex low-temperature phases, including QSL [10–13].

The Co^{2+} ($3d^7$)-based TLAFs are a special class of compounds that manifests various exotic phases of matter similar to the $4f$ systems (e.g., Ce^{3+} and Yb^{3+}) [14–16]. In most of these compounds, the impact of crystal electric field (CEF) and spin-orbit coupling (SOC) in a noncubic environment lead to a Kramers doublet. As a result, the effective magnetic moment of Co^{2+} ions, which possess the true spin $S = 3/2$, can be described by the pseudo-spin $j_{\text{eff}} = 1/2$ at low temperatures, well below the energy scale of the spin-orbit coupling constant (λ/k_B) [17,18]. This allows one to study the combined effects of magnetic frustration and quantum fluctuations due to reduced spin at very low temperatures [19]. In the past few years, a series of triple perovskites with the general formula $A_3\text{CoB}_2\text{O}_9$ ($A = \text{Sr}, \text{Ba}$ and $B = \text{Sb}, \text{Ta}, \text{Nb}$), in which the magnetic Co^{2+} ions are embedded onto 2D triangular layers separated by layers of nonmagnetic A and B atoms, have been rigorously investigated [17,18,20–22]. The most celebrated compound in this family is $\text{Ba}_3\text{CoSb}_2\text{O}_9$, which shows successive magnetic transitions, magnetization plateaus at $1/3$ and $3/5$ of saturation magnetization, and very recently the QSL was claimed [9,17,23]. Several other Co^{2+} -based $j_{\text{eff}} = 1/2$ TLAFs are also reported to show diverse physics with complex magnetic orderings [24–29]. Because of the localized nature of the $3d$ electrons, cobaltates featuring a honeycomb lattice also offer a promising ground to look for Kitaev spin-liquid [30–32]. Indeed, field-induced Kitaev spin-liquid-like behavior has been observed in $\text{Na}_2\text{Co}_2\text{TeO}_6$ [33] and $\text{BaCo}_2(\text{AsO}_4)_2$ [34]. However, their complete phase diagram remains obscure.

*rnath@iisertvm.ac.in

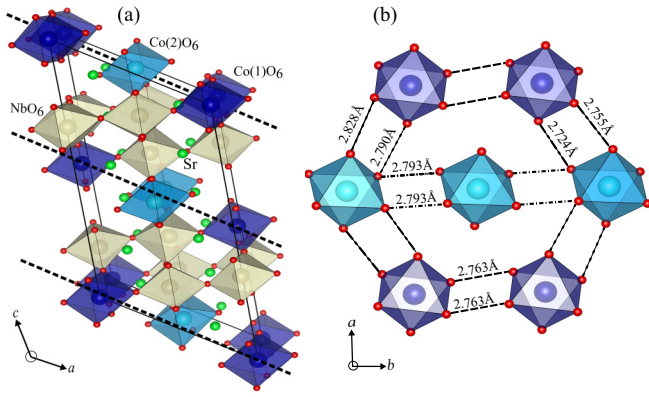


FIG. 1. (a) A three-dimensional view of the crystal structure of $\text{Sr}_3\text{CoNb}_2\text{O}_9$. The dashed lines guide the triangular layers composed of corner-shared CoO_6 and NbO_6 octahedra. The $\text{Co}(1)\text{O}_6$ and $\text{Co}(2)\text{O}_6$ octahedra are shown in different colors. (b) A section of the triangular layer that depicts a nearly parallel edge-shared arrangement of CoO_6 octahedra and presents the honeycomb lattice, after removing NbO_6 octahedra.

In this work, we report a comprehensive study of the synthesis and thermodynamic properties of two new frustrated $j_{\text{eff}} = 1/2$ isostructural TLAFs, $\text{Sr}_3\text{CoNb}_2\text{O}_9$ and $\text{Sr}_3\text{CoTa}_2\text{O}_9$. $\text{Sr}_3\text{CoNb}_2\text{O}_9$ is reported to crystallize in a monoclinic structure with space group $P2_1/c$ [35,36]. Its crystal structure is illustrated in Fig. 1. There are two inequivalent Co atoms residing at the $\text{Co}(1) 2a(0,0,0)$ and $\text{Co}(2) 2d(1/2,1/2,0)$ sites, respectively, which are coordinated with O atoms forming slightly distorted CoO_6 octahedra. Two-dimensional triangular layers are formed by the corner sharing of magnetic CoO_6 and nonmagnetic NbO_6 octahedra in the ab -plane. Figure 1(b) presents nearly parallel edge-sharing CoO_6 octahedra (NbO_6 omitted) displaying possible superimposed honeycomb lattices. The nonmagnetic Sr atoms are located at the interstitial positions. In each layer, an isosceles triangular unit is made up of either one $\text{Co}(1)^{2+}$ and two $\text{Co}(2)^{2+}$ or two $\text{Co}(1)^{2+}$ and one $\text{Co}(2)^{2+}$ ions. Moreover, the Co^{2+} triangular layers are arranged in an AAA-type stacking perpendicular to the c -axis, which results in minuscule interlayer frustration [37]. Magnetic measurements reveal double transitions at low temperatures typical for compounds with easy-axis anisotropy. Despite structural similarity, $\text{Sr}_3\text{CoNb}_2\text{O}_9$ exhibits a $1/3$ magnetization plateau which is absent for $\text{Sr}_3\text{CoTa}_2\text{O}_9$. Further, $\text{Sr}_3\text{CoTa}_2\text{O}_9$ manifests an extended field-induced critical regime where the ground state appears to be of QSL-type while this regime is found to be narrow for $\text{Sr}_3\text{CoNb}_2\text{O}_9$.

II. EXPERIMENTAL DETAILS

Polycrystalline samples of $\text{Sr}_3\text{CoNb}_2\text{O}_9$ and $\text{Sr}_3\text{CoTa}_2\text{O}_9$ were synthesized by the traditional solid-state reaction method. Stoichiometric amounts of SrCO_3 (99.99%, Sigma Aldrich), CoO (99.999%, Sigma Aldrich), and $\text{Nb}_2\text{O}_5/\text{Ta}_2\text{O}_5$ (99.999%, Sigma Aldrich) were mixed and ground thoroughly for 3 h. The mixtures were pressed into disk-shaped pellets and sintered at 1100°C for 24 h. In the next step, the heat treatment was repeated at 1250°C for 24 h after regrinding and repelletization. The powder x-ray diffraction (XRD) was

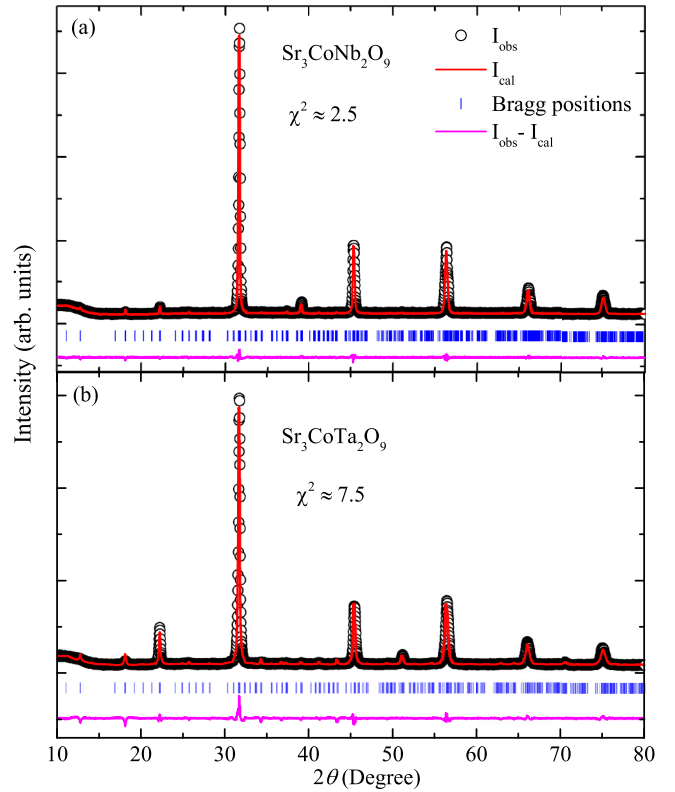


FIG. 2. Room-temperature powder XRD patterns of (a) $\text{Sr}_3\text{CoNb}_2\text{O}_9$ and (b) $\text{Sr}_3\text{CoTa}_2\text{O}_9$. The black circles show the XRD data, and the red line represents the calculated pattern. The blue small vertical lines represent the Bragg positions. The green line at the bottom represents the difference between observed and calculated intensities.

recorded using a PANalytical powder diffractometer ($\text{Cu } K\alpha$ radiation, $\lambda = 1.54182 \text{ \AA}$) at room temperature. Rietveld refinement of the powder XRD data for both compounds was carried out using the FULLPROF software package [38] to check the phase purity of the samples and to calculate the structural parameters.

The dc magnetization (M) measurement was performed with a superconducting quantum interference device (SQUID, MPMS-3, Quantum Design) magnetometer as a function of temperature ($1.8 \leq T \leq 350 \text{ K}$) and magnetic field ($0 \leq H \leq 7 \text{ T}$). High-field magnetization $M(H)$ was measured in a pulsed magnetic field at the Dresden High Magnetic Field Laboratory [39]. Heat capacity (C_p) as a function of T ($0.1 \leq T \leq 300 \text{ K}$) and H ($0 \leq H \leq 9 \text{ T}$) was measured using a thermal relaxation technique in a physical property measurement system (PPMS, Evercool-II, Quantum Design). For $\text{Sr}_3\text{CoNb}_2\text{O}_9$ and $\text{Sr}_3\text{CoTa}_2\text{O}_9$, the measurements were performed down to 0.4 and 0.1 K using ^3He and dilution inserts, respectively, in PPMS.

III. RESULTS

A. Powder x-ray diffraction

Powder XRD data collected at room temperature for $\text{Sr}_3\text{CoNb}_2\text{O}_9$ and $\text{Sr}_3\text{CoTa}_2\text{O}_9$ are shown in Figs. 2(a) and 2(b), respectively. With the help of Rietveld refinement, all

TABLE I. Lattice parameters obtained from the Rietveld refinement of the room-temperature powder XRD data of $\text{Sr}_3\text{Co}(\text{Nb}, \text{Ta})_2\text{O}_9$ (monoclinic, $P2_1/c$).

Parameters	$\text{Sr}_3\text{CoNb}_2\text{O}_9$	$\text{Sr}_3\text{CoTa}_2\text{O}_9$
a (Å)	9.7867(5)	9.7790(5)
b (Å)	5.6460(2)	5.6643(4)
c (Å)	17.0057(4)	16.957(1)
β (deg)	125.32(3)	125.20(3)
V_{cell} (Å ³)	766.67(5)	767.46(8)
Bragg R -factor	2.2	11
Rf-factor	6.5	6.0
χ^2	2.5	7.7
Co(1)-Co(1) (Å)	5.6460(1)	5.6644(5)
Co(2)-Co(2) (Å)	5.6460(1)	5.6644(5)
Co(1)-Co(2) (Å)	5.6493(3)	5.6505(3)

the peaks could be modeled assuming monoclinic structure ($P2_1/c$) for both compounds and taking initial parameters from Refs. [35,36]. This suggests that the new compound obtained replacing Nb by Ta also stabilizes in the same crystal structure. During refinement, the positions of oxygen atoms for $\text{Sr}_3\text{CoTa}_2\text{O}_9$ could not be refined and kept fixed to the values of $\text{Sr}_3\text{CoNb}_2\text{O}_9$. For a comparison, the refined lattice parameters and atomic positions for both compounds are tabulated in Tables I and II, respectively. The obtained structural parameters for $\text{Sr}_3\text{CoNb}_2\text{O}_9$ are in close agreement with the previous reports [35,36].

Upon replacing Nb by Ta, the lattice constants a and c are found to decrease while b increases. This results in an overall increase in the unit-cell volume (V_{cell}). In the crystal structure, all the magnetic Co^{2+} layers are equally spaced with an interlayer separation of ~ 17.0057 and ~ 16.9574 Å for $\text{Sr}_3\text{CoNb}_2\text{O}_9$ and $\text{Sr}_3\text{CoTa}_2\text{O}_9$, respectively.

B. Magnetization

Temperature dependent magnetic susceptibility χ ($\equiv M/H$) of $\text{Sr}_3\text{CoNb}_2\text{O}_9$ and $\text{Sr}_3\text{CoTa}_2\text{O}_9$ measured in a magnetic field of $H = 10$ kOe is shown in Figs. 3(a) and 3(b), respectively. As the temperature is lowered, $\chi(T)$ increases in a Curie-Weiss (CW) manner. No clear indication of any magnetic LRO is observed down to 2 K. When the inverse susceptibility ($1/\chi$) is plotted against temperature, it exhibits a linear behavior at high temperatures and a change in slope at around ~ 50 K. This change in slope is a possible indication of the crossover of the spin state of Co^{2+} from a high-temperature $S = 3/2$ state to an effective $j_{\text{eff}} = 1/2$ ground state [24,28,40]. To extract the magnetic parameters, $1/\chi$ in the low- and high-temperature linear regions is fitted by the modified CW law

$$\chi(T) = \chi_0 + \frac{C}{T - \theta_{\text{CW}}}, \quad (1)$$

where χ_0 represents the temperature-independent susceptibility, C is the CW constant, and θ_{CW} is the characteristic CW temperature. The fit in the high-temperature ($T > 200$ K) range yields ($\chi_0 \simeq 5.315 \times 10^{-4}$ cm³/mol, $C \simeq 3.37$ cm³ K/mol, and $\theta_{\text{CW}} \simeq -24$ K) and ($\chi_0 \simeq 2.84 \times 10^{-4}$ cm³/mol, $C \simeq 3.24$ cm³ K/mol, and $\theta_{\text{CW}} \simeq -21.2$ K)

TABLE II. Atomic positions obtained from the Rietveld refinement of the room-temperature powder XRD data of $\text{Sr}_3\text{Co}(\text{Nb}, \text{Ta})_2\text{O}_9$.

Atom	Wyckoff	x	y	z	Occ.
Sr1	4e	0.2500	0.500	0.08321(6)	1.0
		0.2500	0.500	0.0803(7)	1.0
Sr2	4e	0.7500	0.000	0.08262(3)	1.0
		0.7500	0.000	0.07348(3)	1.0
Sr3	4e	0.2500	0.00	0.2500	1.0
		0.2500	0.00	0.2500	1.0
Co1	2a	0.000	0.000	0.000	0.5
		0.000	0.000	0.000	0.5
Co2	2d	0.500	0.500	0.000	0.5
		0.500	0.500	0.000	0.5
Nb1	4e	0.50949(5)	0.500	0.33735(3)	1.0
Ta1		0.51011(3)	0.500	0.33661(7)	1.0
Nb2	4e	0.00710(4)	0.500	0.16336(8)	1.0
Ta2		0.00975(4)	0.500	0.16713(6)	1.0
O1	4e	0.97200(3)	0.74250(1)	0.2430(6)	1.0
		0.97200(3)	0.74250(1)	0.2430(6)	1.0
O2	4e	0.5260(3)	0.78710(5)	0.27160(6)	1.0
		0.5260(3)	0.78710(5)	0.27160(6)	1.0
O3	4e	0.2500(0)	0.5528(4)	0.26260(2)	1.0
		0.2500(0)	0.5528(4)	0.26260(2)	1.0
O4	4e	0.97210(9)	0.7330(7)	0.90670(4)	1.0
		0.97210(9)	0.7330(7)	0.90670(4)	1.0
O5	4e	0.0279(6)	0.2518(6)	0.92020(5)	1.0
		0.0279(6)	0.2518(6)	0.92020(5)	1.0
O6	4e	0.4721(6)	0.2777(0)	0.89190(1)	1.0
		0.4721(6)	0.2777(0)	0.89190(1)	1.0
O7	4e	0.52790(9)	0.79650(6)	0.9352(5)	1.0
		0.52790(9)	0.79650(6)	0.9352(5)	1.0
O8	4e	0.74060(8)	0.04280(5)	0.9110(3)	1.0
		0.74060(8)	0.04280(5)	0.9110(3)	1.0
O9	4e	0.24060(7)	0.5428(0)	0.90780(3)	1.0
		0.24060(7)	0.5428(0)	0.90780(3)	1.0

for $\text{Sr}_3\text{CoNb}_2\text{O}_9$ and $\text{Sr}_3\text{CoTa}_2\text{O}_9$, respectively. These values of C correspond to an effective moment ($\mu_{\text{eff}} = \sqrt{3k_{\text{B}}C/N_{\text{A}}}$, where N_{A} is the Avogadro number and k_{B} is the Boltzmann constant) of $\mu_{\text{eff}} \simeq 5.2\mu_{\text{B}}$ and $\sim 5.1\mu_{\text{B}}$, respectively, which are close to the expected spin-only value for an $S = 3/2$ Co^{2+} ion.

Similarly, the CW fit [Eq. (1)] to the $1/\chi$ data was performed in the low-temperature region by varying the fitting range between 20 and 60 K. The obtained parameters are [$C \simeq 1.85(5)$ cm³ K/mol and $\theta_{\text{CW}} \simeq -7.5(5)$ K] and [$C \simeq 1.93(3)$ cm³ K/mol and $\theta_{\text{CW}} \simeq -8(1)$ K] for $\text{Sr}_3\text{CoNb}_2\text{O}_9$ and $\text{Sr}_3\text{CoTa}_2\text{O}_9$, respectively. During the fitting procedure, χ_0 was fixed to the Van-Vleck susceptibility (χ_{VV}) obtained from the high-field magnetization data (discussed later). To visualize the low-temperature linear behavior, we have plotted $1/(\chi - \chi_{\text{VV}})$ versus T in the right y-axis for both compounds. These values of C provide the effective magnetic moment of $\mu_{\text{eff}} \simeq 3.84(1)\mu_{\text{B}}$ and $3.92(2)\mu_{\text{B}}$ for Nb and Ta compounds, respectively, which are indeed close to the value expected for

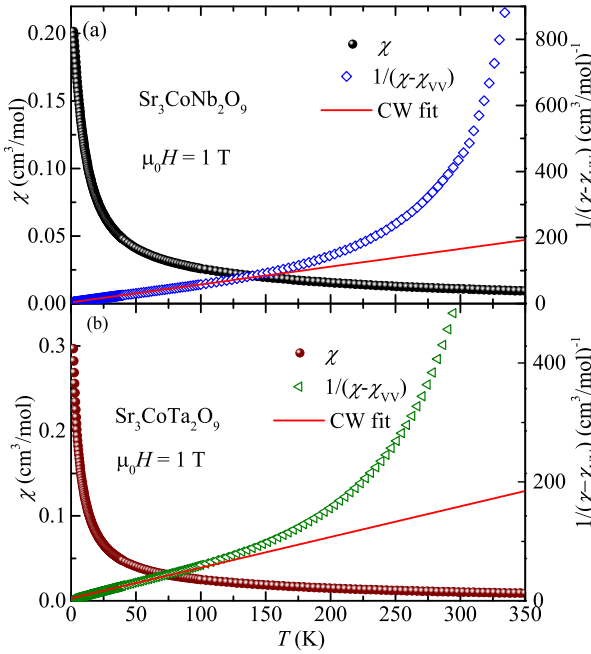


FIG. 3. χ vs T measured in $\mu_0 H = 1$ T for (a) Sr₃CoNb₂O₉ and (b) Sr₃CoTa₂O₉. $1/\chi$ after subtracting χ_{VV} is plotted as a function of T in the right y-axis to emphasize the low- T linear portion. Solid line represents the Curie-Weiss fit in the low-temperature linear regime, as discussed in the text.

$j_{\text{eff}} = 1/2$, assuming $g = 4$. Such a large value of g is not unusual and is typically observed for Co²⁺ systems from the electron-spin-resonance (ESR) experiments due to dominant spin-orbit coupling at low temperatures [17,41]. The negative value of θ_{CW} indicates that the dominant interaction between the spins is AFM in nature.

In a spin system, θ_{CW} is a measure of the exchange coupling and is given by $\theta_{\text{CW}} = [-zJS(S+1)]/3k_B$, where J is the nearest-neighbor (NN) exchange coupling with the Heisenberg Hamiltonian $H = J \sum S_i \cdot S_j$, and z is the number of NN spins [42]. As both compounds have triangular geometry, we have $z = 6$. Thus, using the value of θ_{CW} , z , and j_{eff} in place of S in the above expression, we obtained $J/k_B \simeq 5$ and 5.3 K for Sr₃CoNb₂O₉ and Sr₃CoTa₂O₉, respectively.

Further validation of the $j_{\text{eff}} = 1/2$ ground state and the estimation of exchange coupling were obtained from the high-field magnetization data. The high-field magnetization measured as a function of field up to 60 T using the pulsed magnetic field at a base temperature of $T = 1.4$ K is shown in Figs. 4(a) and 4(b) for Sr₃CoNb₂O₉ and Sr₃CoTa₂O₉, respectively. The pulsed field data are scaled with respect to the magnetization data measured in the SQUID magnetometer up to 7 T at $T = 1.8$ K [43]. For Sr₃CoNb₂O₉, M increases linearly with H and then shows a sharp bend at the saturation field $H_S \simeq 7.2$ T. Such a sharp bend in the powder sample demonstrates an isotropic g -factor and/or exchange interaction, as in the case of Ba₃Co(Nb, Sb)₂O₉ [17,21]. For $H > 8$ T, though it shows a tendency toward saturation, there is still a slow increase. This slow increase of magnetization above H_S is attributed to the temperature-independent Van-Vleck paramagnetism associated with the Co²⁺ ion in the noncubic environment [18]. The slope of a linear fit for $H >$

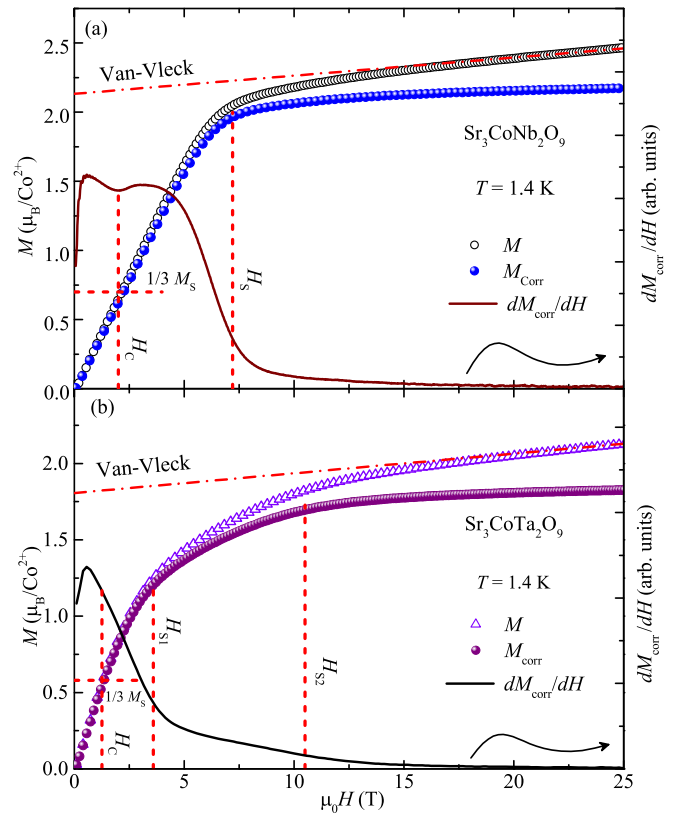


FIG. 4. Magnetization (M) vs H measured at $T = 1.4$ K using pulsed magnetic field for (a) Sr₃CoNb₂O₉ and (b) Sr₃CoTa₂O₉. The dash-dotted line represents the linear fit to the data in high fields, which is extrapolated down to zero field to obtain the Van-Vleck magnetization. The corrected magnetization M_{corr} after the subtraction of the Van-Vleck contribution is also plotted vs H . The dashed lines mark the critical fields. dM_{corr}/dH vs H is plotted in the right y-axis to highlight the features at the critical fields.

15 T and its intercept in the y-axis result in the Van-Vleck paramagnetic susceptibility $\chi_{\text{VV}} \simeq 7.32 \times 10^{-3}$ cm³/mol and saturation magnetization $M_S \simeq 2.13 \mu_B/\text{Co}^{2+}$, respectively. Using this value of M_S , the g -factor ($M_S = gS\mu_B$) is calculated to be $g \simeq 4.26$, assuming $j_{\text{eff}} = 1/2$. A similar g -value is also reported for other Co²⁺ based $j_{\text{eff}} = 1/2$ TLAFs [18,20,22,28]. The corrected magnetization (M_{corr}) after subtracting the Van-Vleck contribution is also plotted in the same graph. To precisely pinpoint the saturation field, we have plotted the derivative dM_{corr}/dH versus H in the right y-axis. The curve exhibits a valley at $H \simeq 2$ T, which corresponds to $1/3$ of M_S and then a sharp drop at $\mu_0 H_S \simeq 7.2$ T (or a slope change in the M_{corr} versus H curve), indicating the saturation field or critical field above which the spin system attains the fully polarized state [18].

Unlike Sr₃CoNb₂O₉, the magnetic behavior of Sr₃CoTa₂O₉ is found to be somewhat different. Magnetization shows a broad bend between two critical fields $\mu_0 H_{S1} \simeq 3.6$ T and $\mu_0 H_{S2} \simeq 10.5$ T. Above H_{S2} , the magnetization saturates but there is still a slow increase, similar to Sr₃CoNb₂O₉. A straight line fit above 20 T yields $\chi_{\text{VV}} \simeq 7.2 \times 10^{-3}$ cm³/mol and $M_S \simeq 1.8 \mu_B/\text{Co}^{2+}$. This value of M_S corresponds to $g \simeq 3.6$ with $j_{\text{eff}} = 1/2$. The Van-Vleck corrected magnetization

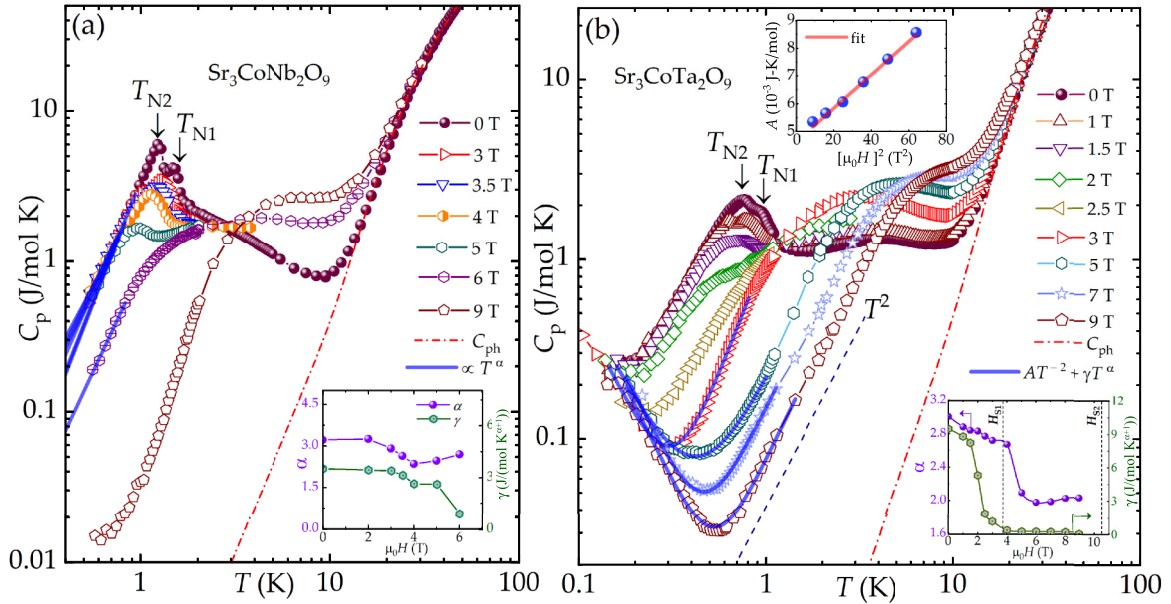


FIG. 5. Temperature-dependent heat capacity [$C_p(T)$] measured in different magnetic fields for (a) $\text{Sr}_3\text{CoNb}_2\text{O}_9$ and (b) $\text{Sr}_3\text{CoTa}_2\text{O}_9$. The red dash-dotted line represents the lattice heat capacity using Eq. (2). The black solid lines are the power law and power law+nuclear Schottky fits to the low- T data of $\text{Sr}_3\text{CoNb}_2\text{O}_9$ and $\text{Sr}_3\text{CoTa}_2\text{O}_9$, respectively. The dashed line in (b) marks the power law with $\alpha = 2$. Lower insets: Variation of α and γ with H in the left and right y-axes, respectively, obtained from the low-temperature data fit. Upper inset in (b) is the plot of A vs H^2 , with the solid line being a linear fit.

M_{corr} and its derivative dM_{corr}/dH as a function of H are plotted in the left and right y-axes, respectively, in Fig. 4(b), which show pronounced features at H_{S1} and H_{S2} . These features are quite different from the broad contour expected due to g -factor anisotropy. This is an indication of the existence of an exotic field-induced state between H_{S1} and H_{S2} , similar to $\text{Na}_2\text{Co}_2\text{TeO}_6$ [33]. No obvious feature is seen at the field corresponding to the $1/3$ magnetization.

The saturation field defines the energy required to overcome the antiferromagnetic exchange energy and polarize the spins in the direction of magnetic field. In particular, in a Heisenberg TLAF, H_S can be written in terms of the intralayer exchange coupling as $\mu_0 H_S = 9JS/g\mu_B$ [44]. For $\text{Sr}_3\text{CoNb}_2\text{O}_9$, our experimental value of $\mu_0 H_S \simeq 7.2$ T yields an average exchange coupling of $J/k_B \simeq 4.7$ K. Similarly, for $\text{Sr}_3\text{CoTa}_2\text{O}_9$, $\mu_0 H_{S2} \simeq 10.5$ T gives $J/k_B \simeq 5.8$ K. These values of J/k_B are in reasonable agreement with those obtained from the analysis of θ_{CW} . The slight difference in magnitude can be attributed to the magnetic anisotropy present in the compounds.

Heisenberg TLAFs typically show a $1/3$ magnetization plateau in an intermediate field range where the spins evolve from a conventional 120° spin structure to a *uud* state [45–47]. Though a weak anomaly is visible for $\text{Sr}_3\text{CoNb}_2\text{O}_9$, it is completely smeared for $\text{Sr}_3\text{CoTa}_2\text{O}_9$. The absence of a $1/3$ magnetization plateau is likely due to the polycrystalline nature of the sample, where random orientation of the crystallites averages out this effect. Moreover, our $M(H)$ is measured at $T = 1.4$ K (above T_{N1}), at which the impact of magnetic anisotropy is minimal. Therefore, $M(H)$ measurement below T_{N2} would reveal these features more clearly.

C. Heat capacity

To delineate the low-energy excitations, temperature-dependent heat capacity [$C_p(T)$] measured in different applied fields is shown in Figs. 5(a) and 5(b) for $\text{Sr}_3\text{CoNb}_2\text{O}_9$ and $\text{Sr}_3\text{CoTa}_2\text{O}_9$, respectively. The overall temperature variation of C_p for both compounds is found to be nearly the same. In zero-field, as the temperature decreases, C_p decreases monotonically, and below ~ 10 K it displays a weak and broad maximum, a possible indication of short-range ordering due to two-dimensionality of the spin lattice. With further decrease in temperature, two well-defined peaks appear at $T_{N1} \simeq 1.47$ K and $T_{N2} \simeq 1.22$ K for $\text{Sr}_3\text{CoNb}_2\text{O}_9$ and at $T_{N1} \simeq 0.88$ K and $T_{N2} \simeq 0.67$ K for $\text{Sr}_3\text{CoTa}_2\text{O}_9$, indicating the onset of two successive magnetic transitions at low temperatures. When external magnetic field is applied, the height of the peaks is reduced substantially and the peak positions shift towards low temperatures. At higher fields, both transition peaks are merged into a broad peak and gradually vanish from the measurement window. This reflects the AFM nature of both transitions. In addition, as the field increases, the broad maximum initially shifts towards low temperatures as expected for a short-range magnetic order. For higher fields, the position of the maximum shifts in the reverse direction (to high temperatures), its height increases, and it shows a drastic broadening, reminiscent of a Schottky anomaly due to CEF splitting. Furthermore, the zero-field $C_p(T)$ of $\text{Sr}_3\text{CoTa}_2\text{O}_9$ shows an upturn below ~ 0.2 K which moves towards high temperatures with increasing field. This is a typical behavior of nuclear Schottky arising due to a quadrupole splitting of ^{59}Co ($I = 7/2$) nuclear levels [48].

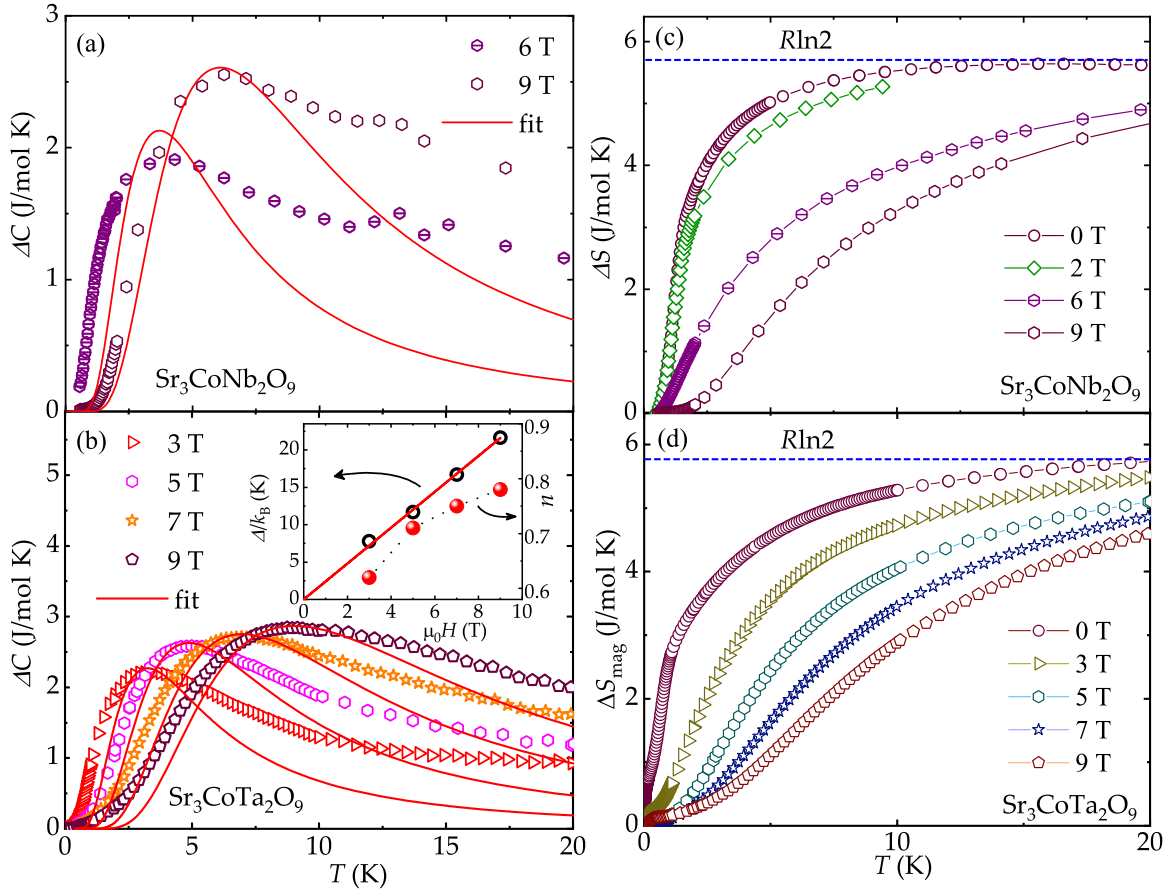


FIG. 6. Difference in heat capacity $\Delta C (= C_p - C_{ph} - C_n)$ vs T in different magnetic fields for (a) $\text{Sr}_3\text{CoNb}_2\text{O}_9$ and (b) $\text{Sr}_3\text{CoTa}_2\text{O}_9$. The solid lines are the fits using Eq. (5). The inset of (b) shows the plot of Δ/k_B and n as a function of H for $\text{Sr}_3\text{CoTa}_2\text{O}_9$ in the left and right y-axes, respectively. The change in magnetic entropy ΔS vs T in different magnetic fields for (c) $\text{Sr}_3\text{CoNb}_2\text{O}_9$ and (d) $\text{Sr}_3\text{CoTa}_2\text{O}_9$.

In a magnetic insulator, C_p in zero-field has three major contributions: lattice heat capacity (C_{ph}) due to phonon vibrations, which usually dominates at high temperatures; magnetic heat capacity (C_{mag}) due to spins, which becomes predominant at low temperatures; and the nuclear Schottky contribution (C_n), which is effective only at very low temperatures (below $\sim 10^{-2}$ K). In the absence of a nonmagnetic analog, $C_{ph}(T)$ is evaluated by fitting $C_p(T)$ in the high-temperature region by a linear combination of one Debye and four Einstein terms [49],

$$C_{ph}(T) = f_D C_D(\theta_D, T) + \sum_{i=1}^4 g_i C_{E_i}(\theta_{E_i}, T). \quad (2)$$

The first term in Eq. (2) is the Debye model,

$$C_D(\theta_D, T) = 9nR \left(\frac{T}{\theta_D} \right)^3 \int_0^{\frac{\theta_D}{T}} \frac{x^4 e^x}{(e^x - 1)^2} dx, \quad (3)$$

where R is the universal gas constant, n is the number of atoms in the formula unit, and θ_D is the characteristic Debye temperature. The flat optical modes in the phonon spectra are accounted for by the second term in Eq. (2), called the Einstein term,

$$C_E(\theta_E, T) = 3nR \left(\frac{\theta_E}{T} \right)^2 \frac{e^{\left(\frac{\theta_E}{T}\right)}}{\left[e^{\left(\frac{\theta_E}{T}\right)} - 1 \right]^2}, \quad (4)$$

where θ_E is the characteristic Einstein temperature. The coefficients f_D , g_1 , g_2 , g_3 , and g_4 are the weight factors, which take into account the number of atoms per formula unit (n), and they are chosen in such a way that $f_D + g_1 + g_2 + g_3 + g_4 = 1$ and the Dulong-Petit value ($\sim 3nR$) is satisfied at high temperatures.

The zero-field $C_p(T)$ above 40 K is fitted by Eq. (2), and the obtained fitting parameters are ($f_D \simeq 0.066$, $g_1 \simeq 0.066$, $g_2 \simeq 0.20$, $g_3 \simeq 0.13$, $g_4 \simeq 0.533$, $\theta_D \simeq 178$ K, $\theta_{E1} \simeq 117$ K, $\theta_{E2} \simeq 206$ K, $\theta_{E3} \simeq 328$ K, and $\theta_{E4} \simeq 520$ K) and ($f_D \simeq 0.066$, $g_1 \simeq 0.066$, $g_2 \simeq 0.20$, $g_3 \simeq 0.13$, $g_4 \simeq 0.533$, $\theta_D \simeq 163$ K, $\theta_{E1} \simeq 117$ K, $\theta_{E2} \simeq 195$ K, $\theta_{E3} \simeq 294$ K, and $\theta_{E4} \simeq 490$ K) for $\text{Sr}_3\text{CoNb}_2\text{O}_9$ and $\text{Sr}_3\text{CoTa}_2\text{O}_9$, respectively. The fit was extrapolated down to the lowest measured temperature (see Fig. 5) to obtain $C_{ph}(T)$. The estimation of C_n is discussed later. The magnetic and/or Schottky contributions, ΔC , obtained by subtracting C_{ph} and C_n from total C_p are plotted as a function of T for different fields in Figs. 6(a) and 6(b) for the Nb and Ta compounds, respectively. The respective changes in magnetic entropies evaluated by integrating $\Delta C/T$ with respect to T [i.e., $\Delta S = \int_0^T \frac{\Delta C(T')}{T'} dT'$] for different fields are shown in Figs. 6(c) and 6(d). The saturation value of ΔS approaches $R \ln 2$ above ~ 30 K irrespective of the value of applied field for both compounds, further evidencing the $j_{\text{eff}} = 1/2$ ground state for Co^{2+} .

$\Delta C(T)$ in different fields can be fitted by the following two-level Schottky function:

$$C_S = n_S R \left(\frac{\Delta}{k_B T} \right)^2 \frac{e^{-\frac{\Delta}{k_B T}}}{\left(1 + e^{-\frac{\Delta}{k_B T}} \right)^2}, \quad (5)$$

where n_S is the number of free spins per formula unit contributing to the Schottky behavior, and Δ/k_B is the Zeeman gap in magnetic fields. We fitted the data in different magnetic fields by Eq. (5) making n and Δ/k_B fitting parameters [Figs. 6(a) and 6(b)]. The fit reproduces the experimental data reasonably well, especially in the broad maximum regime. However, the deviation in the high-temperature regime can be ascribed to the unreliable subtraction of the phonon contribution and the presence of the magnetic contribution. The obtained Δ/k_B and n are plotted as a function of field in the inset of Fig. 6(b) for $\text{Sr}_3\text{CoTa}_2\text{O}_9$. With increasing H , n increases systematically, suggesting the excitation of more free spins to the higher energy levels. It is expected to reach the maximum value (~ 1) in the fully polarized state, above $H_{S2} \simeq 10.5$ T. Similarly, Δ/k_B varies linearly with H . Taking the value of $\Delta/k_B \simeq 21.65$ K at $H = 9$ T, which is close to the saturation field, we obtained $g \simeq 3.58$. This value of g is indeed close to that obtained from the magnetization analysis. This further elucidates that the Schottky effect in heat capacity is arising from the Co^{2+} Kramers doublet with $j_{\text{eff}} = 1/2$.

IV. DISCUSSION

For both compounds, double magnetic transitions are observed at T_{N1} and T_{N2} ($T_{N2} < T_{N1}$) in zero-field. It is predicted that double transitions can occur in TLAFs when the magnetic anisotropy is of easy-axis type, while the TLAFs with easy-plane type anisotropy may show only a single transition [50–53]. Upon lowering the temperature, the collinear *uud* state appears before the 120° state in TLAFs with easy-axis anisotropy. When magnetic field is applied, an additional high-field 2:1 canted phase is also stabilized [46]. The temperature range of the intermediate phase ($T_{N1} - T_{N2}$)/ T_{N1} reflects the relative strength of easy-axis anisotropy with respect to the isotropic intralayer coupling. Similar types of double transitions are reported for $\text{Ba}_3\text{Co}(\text{Nb}, \text{Ta}, \text{Sb})_2\text{O}_9$ and some other compounds [20–23,23]. Thus, the two consecutive magnetic transitions at low temperatures are attributed to the easy-axis anisotropy in both of our compounds, and the 120° ordering below T_{N2} is preceded by a collinear order between T_{N1} and T_{N2} . The observed narrow temperature regime between T_{N1} and T_{N2} in both compounds suggests considerably weak anisotropy compared to the isotropic exchange coupling in the Hamiltonian [18]. This implies that these compounds are closer to the Heisenberg model in contrast to strong anisotropy anticipated for Co-based compounds [54], and the local environment of Co^{2+} is close to a cubic symmetry as in KCoF_3 and $\text{Ba}_3\text{CoSb}_2\text{O}_9$ [18]. Recent theoretical studies claim that the Heisenberg model on a triangular lattice with no anisotropy can also show a double phase transition [46]. It is also suggested that the transition from *uud* to the 120° state (at T_{N2}) can be described by the conventional Berezinskii-Kosterlitz-Thouless (BKT) universality class. The magnetic (T - H) phase diagram constructed using the transition temperatures from $C_p(T)$ and the saturation fields from

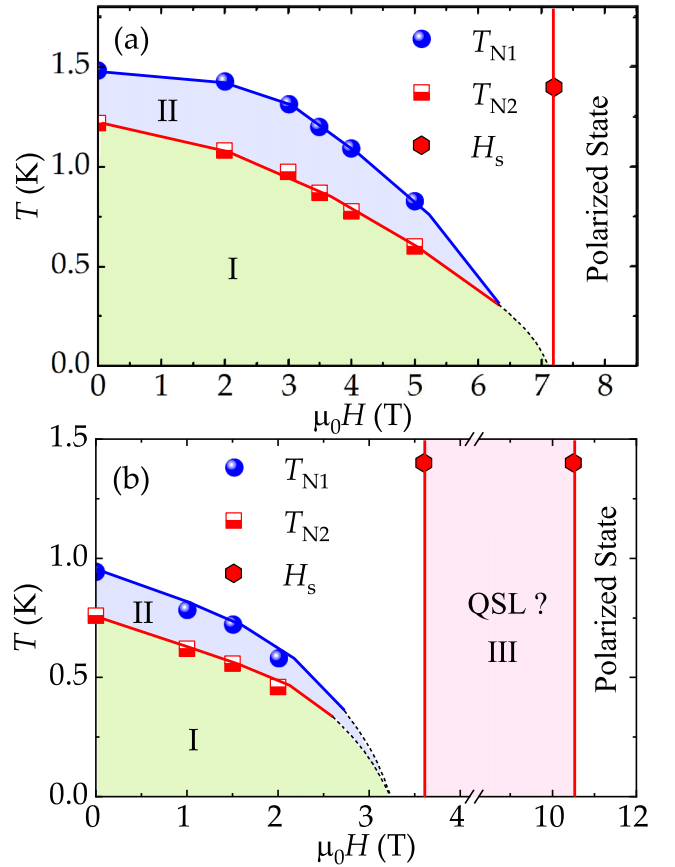


FIG. 7. T vs H phase diagram for (a) $\text{Sr}_3\text{CoNb}_2\text{O}_9$ and (b) $\text{Sr}_3\text{CoTa}_2\text{O}_9$ constructed using the heat capacity and magnetization data. The exotic-field induced regime (III) between H_{S1} and H_{S2} for $\text{Sr}_3\text{CoTa}_2\text{O}_9$ is highlighted in a different color.

the magnetization data are presented in Figs. 7(a) and 7(b) for $\text{Sr}_3\text{CoNb}_2\text{O}_9$ and $\text{Sr}_3\text{CoTa}_2\text{O}_9$, respectively. Both compounds exhibit two common phase regimes I and II known to be 120° and collinear spin states, respectively, as typically observed in the majority of TLAFs. Upon increasing the field, both transitions are merged into one and are expected to approach zero temperature at around ~ 7 T for $\text{Sr}_3\text{CoNb}_2\text{O}_9$ and ~ 3 T for $\text{Sr}_3\text{CoTa}_2\text{O}_9$, respectively. These fields are very close to their respective saturation fields.

The most striking difference between these two compounds is that $\text{Sr}_3\text{CoTa}_2\text{O}_9$ shows the appearance of an exotic phase in an extended field range [regime III in Fig. 7(b)] while for $\text{Sr}_3\text{CoNb}_2\text{O}_9$ this phase is either absent or exists over a narrow field range. To understand the peculiar behavior in the magnetization data, we fitted $C_p(T)$ in the low-temperature regime by a power law of the form $C_p = \gamma T^\alpha$ for $\text{Sr}_3\text{CoNb}_2\text{O}_9$. To accommodate the low- T upturn, $C_p(T)$ data of $\text{Sr}_3\text{CoTa}_2\text{O}_9$ were fitted with a sum of A/T^2 and γT^α from the lowest temperature to 1 K [55]. Here, A/T^2 accounts for the high-temperature part of the nuclear Schottky anomaly, which is merely the high-temperature approximation of Eq. (5) [56]. The constant A is related to the nuclear level splitting Δ (both quadrupolar and Zeeman) with $A \propto \Delta^2$ for $T \gg \Delta$. A is found to increase quadratically with H [upper inset of Fig. 5(b)], which is consistent with the theoretical prediction [48].

The obtained values of γ and α are plotted against H in the lower insets of the respective figures. For $\text{Sr}_3\text{CoNb}_2\text{O}_9$, the value of α is found to be close to 3 for all the measured fields [inset of Fig. 5(a)], as expected in a 3D AFM ordered state. Only at $H = 9$ T, which is well above H_S , the fitted parameters were not reliable, possibly because of large scattering in the low-temperature data and low heat capacity values. On the other hand, for $\text{Sr}_3\text{CoTa}_2\text{O}_9$, the value of α is found to be close to 3 (with $\gamma \simeq 1042$ mJ/mol K^{3.75}) for $H = 3$ T, as expected [lower inset of Fig. 5(b)]. For $H > 4$ T, it is reduced significantly to about ~ 2 and remains almost field-independent. Interestingly, these fields fall within the exotic regime (between $\mu_0 H_{S1} \simeq 3.6$ T and $\mu_0 H_{S2} \simeq 10.5$ T) found from the magnetization measurements. In these fields, the value of γ varies from ~ 300 to 90 mJ/mol K³, which is a significant reduction from the 3 T value, but it is still considerably large.

Typically, one expects a T^3 behavior for $C_p(T)$ due to 3D spin-wave dispersion in the AFM ordered state [57]. On the other hand, a more conventional characteristic feature of QSL is the linear temperature dependency of low temperature $C_p(T)$, i.e., $C_p = \gamma T$, where γ is related to the spinon density of states at the spinon Fermi surface. Likewise, a quadratic temperature dependency ($C_p \propto T^2$) is predicted theoretically for the gapless Dirac QSLs at low temperatures [58,59]. Indeed, several QSL candidates with triangular, kagome, and hyper-kagome geometries are reported to evince such a behavior at low temperatures [55,60–63]. Thus, the suppression of magnetic LRO and power-law behavior of C_p with a reduced value of $\alpha \sim 2$ in the critical field region unambiguously point towards an exotic phase regime, possibly the field-induced QSL in $\text{Sr}_3\text{CoTa}_2\text{O}_9$ [64,65]. Moreover, the obtained large value of γ can also be considered as a generic feature of low-energy gapless excitations, as observed for gapless QSL candidates $\text{Ba}_3\text{CuSb}_2\text{O}_9$ and $\text{Sr}_2\text{Cu}(\text{Te}_{0.5}\text{W}_{0.5})\text{O}_6$ [66].

This type of field-induced behavior is observed in some honeycomb lattices with strong Kitaev interaction. The Kitaev physics demands the presence of bond-dependent anisotropy, which can be realized in honeycomb lattices as well as spin dimers with strong spin-orbit coupling where the metal octahedra are either edge shared or parallelly edge shared [67]. Further, it is predicted that spin-orbit coupled honeycomb systems with $j_{\text{eff}} = 1/2$ are an ideal avenue to host Kitaev spin-liquid [68]. Indeed, $j_{\text{eff}} = 1/2$ honeycomb lattices $\alpha\text{-RuCl}_3$ [69], $\text{Na}_2\text{Co}_2\text{TeO}_6$ [33], $\text{BaCo}_2(\text{AsO}_4)_2$ [34], and $\text{BaCo}_2(\text{P}_{1-x}\text{V}_x)\text{O}_8$ [70] with strong anisotropy show the onset of conventional magnetic LRO at low temperatures. Under magnetic field, the LRO is suppressed (i.e., the anisotropic bond-dependent coupling dominates over the isotropic coupling) and the system eventually crosses over to a low-temperature nonmagnetic or disordered state, which is understood to be the field-induced Kitaev spin-liquid [67]. A triangular lattice can also be viewed as a superposition of honeycomb layers in a certain stacking sequence. This analogy can be extended to the TLAFs $\text{Sr}_3\text{Co}(\text{Nb}, \text{Ta})_2\text{O}_9$. A careful inspection of the crystal structure reveals that the CoO_6 octahedra in both compounds are parallelly edge shared when the nonmagnetic (Nb, Ta) O_6 octahedra are removed. In Fig. 1(b), we have schematized the ways in which parallel edge sharing could be feasible in $\text{Sr}_3\text{Co}(\text{Nb}, \text{Ta})_2\text{O}_9$. As one can clearly

see, the identical Co-octahedra are perfectly parallelly edge shared, which might facilitate a bond-dependent anisotropy and hence Kitaev interaction [10,41]. Meanwhile, due to the low-symmetry crystal structure, there is an inherent distortion in the metal octahedra due to which the edge sharing between two dissimilar octahedra [Co(1) O_6 and Co(2) O_6] is deviating slightly from the perfect parallel edge sharing. It should be noted that the recent theoretical work on TLAFs has also predicted a transition from an ordered magnetic state in the isotropic case into a QSL state in the easy-axis regime, with increasing easy-axis anisotropy [71]. Nevertheless, to conclusively establish this novel phenomenon in these TLAFs, inelastic neutron scattering and μSR experiments in dilution temperatures and under magnetic fields on good quality single crystals would be imperative.

Experimentally, the extent of frustration in any magnetically frustrated material is quantified by the frustration ratio $f = |\theta_{\text{CW}}|/T_N$ [72]. From the value of θ_{CW} and T_{N1} , the frustration parameter is calculated to be $f \sim 5$ and ~ 9 for $\text{Sr}_3\text{CoNb}_2\text{O}_9$ and $\text{Sr}_3\text{CoTa}_2\text{O}_9$, respectively. Despite the same crystal structure, the latter shows stronger frustration and a fluctuating regime over an extended field range, while for the former, the extent of frustration is less and hence the fluctuating regime is narrowed. The possible origin of such a drastic difference in magnetic properties can be attributed to the hierarchy of the exchange couplings. It should be noted that the $\text{Co}^{2+}-\text{Co}^{2+}$ superexchange involves $\text{Co}^{2+}(3d)-\text{O}^{2-}(2p)-\text{Nb}^{5+}(4p)-\text{O}^{2-}(2p)-\text{Co}^{2+}(3d)$ and $\text{Co}^{2+}(3d)-\text{O}^{2-}(2p)-\text{Ta}^{5+}(4f)-\text{O}^{2-}(2p)-\text{Co}^{2+}(3d)$ pathways for $\text{Sr}_3\text{CoNb}_2\text{O}_9$ and $\text{Sr}_3\text{CoTa}_2\text{O}_9$, respectively. Hence, the difference in coupling strength is likely due to the participation of different orbitals of $\text{Nb}^{5+}(4p)$ and $\text{Ta}^{5+}(4f)$ in the interaction mechanism [21,73].

V. CONCLUSION

We report a detailed study of the thermodynamic properties of two new quantum magnets $\text{Sr}_3\text{Co}(\text{Nb}, \text{Ta})_2\text{O}_9$ possessing Co^{2+} triangular layers. Their low-temperature properties are unequivocally described by a $j_{\text{eff}} = 1/2$ Kramers doublet of Co^{2+} ions interacting antiferromagnetically. Similar to many other TLAFs with easy-axis anisotropy, both compounds undergo two sequential magnetic transitions at low temperatures. $\text{Sr}_3\text{CoNb}_2\text{O}_9$ exhibits a weak plateau-type feature at the 1/3 magnetization, while this feature is smeared for $\text{Sr}_3\text{CoTa}_2\text{O}_9$, likely due to the effect of magnetic anisotropy and/or random orientation of the crystallites. Despite having the same crystal structure, $\text{Sr}_3\text{CoTa}_2\text{O}_9$ with $f \simeq 9$ is found to be more frustrated than $\text{Sr}_3\text{CoNb}_2\text{O}_9$ with $f \simeq 5$, which can be attributed to the involvement of different orbitals of Ta^{5+} and Nb^{5+} in the interaction paths. The existence of an exotic field-induced quantum phase is detected for $\text{Sr}_3\text{CoTa}_2\text{O}_9$ over a wide field range below the fully polarized state, while this behavior is either absent or exists over a narrow field range for the Nb analog. Because of this nontrivial character, $\text{Sr}_3\text{CoTa}_2\text{O}_9$ is a model system for further experimental as well as theoretical investigations at low temperatures and under magnetic fields.

Note added. During the course of our work, we became aware of an independent study on $\text{Sr}_3\text{CoTa}_2\text{O}_9$ [crystal structure: trigonal ($P\bar{3}m1$)] [74]. They also observed double transitions at low temperatures.

ACKNOWLEDGMENTS

We would like to acknowledge SERB, India, for financial support under Grant No. CRG/2022/000997. We also

acknowledge the support of HLD-HZDR, member of the European Magnetic Field Laboratory (EMFL). S.J.S. is supported by the Prime Minister's Research Fellowship (PMRF) scheme, Government of India.

- [1] C. Lacroix, P. Mendels, and F. Mila, *Introduction to Frustrated Magnetism: Materials, Experiments, Theory* (Springer-Verlag, Berlin, 2011), Vol. 164.
- [2] H. T. Diep, *Frustrated Spin Systems* (World Scientific, Singapore, 2005).
- [3] L. Balents, Spin liquids in frustrated magnets, *Nature (London)* **464**, 199 (2010); L. Savary and L. Balents, Quantum spin liquids: A review, *Rep. Prog. Phys.* **80**, 016502 (2017).
- [4] P. W. Anderson, Resonating valence bonds: A new kind of insulator?, *Mater. Res. Bull.* **8**, 153 (1973).
- [5] R. R. P. Singh and D. A. Huse, Three-Sublattice Order in Triangular- and Kagomé-Lattice Spin-Half Antiferromagnets, *Phys. Rev. Lett.* **68**, 1766 (1992).
- [6] L. Capriotti, A. E. Trumper, and S. Sorella, Long-Range Néel Order in the Triangular Heisenberg Model, *Phys. Rev. Lett.* **82**, 3899 (1999).
- [7] S. R. White and A. L. Chernyshev, Néel Order in Square and Triangular Lattice Heisenberg Models, *Phys. Rev. Lett.* **99**, 127004 (2007).
- [8] A. V. Chubukov and D. I. Golosov, Quantum theory of an antiferromagnet on a triangular lattice in a magnetic field, *J. Phys.: Condens. Matter* **3**, 69 (1991).
- [9] L. Kamiya, Y. Ge, T. Hong, D. L. Qiu, Y. Quintero-Castro, Z. Lu, H. B. Cao, E. S. Matsuda, M. Choi, C. D. Batista, M. Mourigal, H. D. Zhou, and J. Ma, The nature of spin excitations in the one-third magnetization plateau phase of $\text{Ba}_3\text{CoSb}_2\text{O}_9$, *Nat. Commun.* **9**, 2666 (2018).
- [10] P. A. Maksimov, Z. Zhu, S. R. White, and A. L. Chernyshev, Anisotropic-Exchange Magnets on a Triangular Lattice: Spin Waves, Accidental Degeneracies, and Dual Spin Liquids, *Phys. Rev. X* **9**, 021017 (2019).
- [11] W.-J. Hu, S.-S. Gong, W. Zhu, and D. N. Sheng, Competing spin-liquid states in the spin- $\frac{1}{2}$ Heisenberg model on the triangular lattice, *Phys. Rev. B* **92**, 140403(R) (2015).
- [12] P.-E. Melchy and M. E. Zhitomirsky, Interplay of anisotropy and frustration: Triple transitions in a triangular-lattice antiferromagnet, *Phys. Rev. B* **80**, 064411 (2009).
- [13] K. M. Ranjith, R. Nath, M. Skoulatos, L. Keller, D. Kasinathan, Y. Skourski, and A. A. Tsirlin, Collinear order in the frustrated three-dimensional spin- $\frac{1}{2}$ antiferromagnet $\text{Li}_2\text{CuW}_2\text{O}_8$, *Phys. Rev. B* **92**, 094426 (2015); K. M. Ranjith, M. Majumder, M. Baenitz, A. A. Tsirlin, and R. Nath, Frustrated three-dimensional antiferromagnet $\text{Li}_2\text{CuW}_2\text{O}_8$: ^7Li NMR and the effect of nonmagnetic dilution, *ibid.* **92**, 024422 (2015).
- [14] Y. Li, G. Chen, W. Tong, L. Pi, J. Liu, Z. Yang, X. Wang, and Q. Zhang, Rare-Earth Triangular Lattice Spin Liquid: A Single-Crystal Study of YbMgGaO_4 , *Phys. Rev. Lett.* **115**, 167203 (2015).
- [15] M. M. Bordelon, X. Wang, D. M. Pajerowski, A. Banerjee, M. Sherwin, C. M. Brown, M. S. Eldeeb, T. Petersen, L. Hozoi, U. K. Rößler, M. Mourigal, and S. D. Wilson, Magnetic properties and signatures of moment ordering in the triangular lattice antiferromagnet KCeO_2 , *Phys. Rev. B* **104**, 094421 (2021).
- [16] K. Somesh, S. S. Islam, S. Mohanty, G. Simutis, Z. Guguchia, C. Wang, J. Sichelschmidt, M. Baenitz, and R. Nath, Absence of magnetic order and emergence of unconventional fluctuations in $J_{\text{eff}} = 1/2$ triangular lattice antiferromagnet YbBO_3 , [arXiv:2210.09724](https://arxiv.org/abs/2210.09724).
- [17] T. Susuki, N. Kurita, T. Tanaka, H. Nojiri, A. Matsuo, K. Kindo, and H. Tanaka, Magnetization Process and Collective Excitations in the $S=1/2$ Triangular-Lattice Heisenberg Antiferromagnet $\text{Ba}_3\text{CoSb}_2\text{O}_9$, *Phys. Rev. Lett.* **110**, 267201 (2013).
- [18] Y. Shirata, H. Tanaka, A. Matsuo, and K. Kindo, Experimental Realization of a Spin- $1/2$ Triangular-Lattice Heisenberg Antiferromagnet, *Phys. Rev. Lett.* **108**, 057205 (2012).
- [19] R. Zhong, S. Guo, G. Xu, Z. Xu, and R. J. Cava, Strong quantum fluctuations in a quantum spin liquid candidate with a Co-based triangular lattice, *Proc. Natl. Acad. Sci. USA* **116**, 14505 (2019).
- [20] M. Lee, J. Hwang, E. S. Choi, J. Ma, C. R. Dela Cruz, M. Zhu, X. Ke, Z. L. Dun, and H. D. Zhou, Series of phase transitions and multiferroicity in the quasi-two-dimensional spin- $\frac{1}{2}$ triangular-lattice antiferromagnet $\text{Ba}_3\text{CoNb}_2\text{O}_9$, *Phys. Rev. B* **89**, 104420 (2014).
- [21] K. Yokota, N. Kurita, and H. Tanaka, Magnetic phase diagram of the $S = \frac{1}{2}$ triangular-lattice Heisenberg antiferromagnet $\text{Ba}_3\text{CoNb}_2\text{O}_9$, *Phys. Rev. B* **90**, 014403 (2014).
- [22] K. M. Ranjith, K. Brinda, U. Arjun, N. G. Hegde, and R. Nath, Double phase transition in the triangular antiferromagnet $\text{Ba}_3\text{CoTa}_2\text{O}_9$, *J. Phys.: Condens. Matter* **29**, 115804 (2017).
- [23] H. D. Zhou, C. Xu, A. M. Hallas, H. J. Silverstein, C. R. Wiebe, I. Umegaki, J. Q. Yan, T. P. Murphy, J.-H. Park, Y. Qiu, J. R. D. Copley, J. S. Gardner, and Y. Takano, Successive Phase Transitions and Extended Spin-Excitation Continuum in the $S=\frac{1}{2}$ Triangular-Lattice Antiferromagnet $\text{Ba}_3\text{CoSb}_2\text{O}_9$, *Phys. Rev. Lett.* **109**, 267206 (2012).
- [24] N. Li, Q. Huang, X. Yue, W. Chu, Q. Chen, E. Choi, X. Zhao, H. Zhou, and X. Sun, Possible itinerant excitations and quantum spin state transitions in the effective spin- $1/2$ triangular-lattice antiferromagnet $\text{Na}_2\text{BaCo}(\text{PO}_4)_2$, *Nat. Commun.* **11**, 4216 (2020).
- [25] Y. Kojima, M. Watanabe, N. Kurita, H. Tanaka, A. Matsuo, K. Kindo, and M. Avdeev, Quantum magnetic properties of the spin- $\frac{1}{2}$ triangular-lattice antiferromagnet $\text{Ba}_2\text{La}_2\text{CoTe}_2\text{O}_{12}$, *Phys. Rev. B* **98**, 174406 (2018).
- [26] R. Rawl, M. Lee, E. S. Choi, G. Li, K. W. Chen, R. Baumbach, C. R. de la Cruz, J. Ma, and H. D. Zhou, Magnetic properties of the triangular lattice magnets $A_4B'B_2\text{O}_{12}$ ($A = \text{Ba, Sr, La}$; $B' = \text{Co, Ni, Mn}$; $B = \text{W, Re}$), *Phys. Rev. B* **95**, 174438 (2017).
- [27] R. Zhong, S. Guo, L. T. Nguyen, and R. J. Cava, Frustrated spin- $1/2$ dimer compound $\text{K}_2\text{Co}_2(\text{SeO}_3)_3$ with easy-axis anisotropy, *Phys. Rev. B* **102**, 224430 (2020).

- [28] R. Rawl, L. Ge, H. Agrawal, Y. Kamiya, C. R. de la Cruz, N. P. Butch, X. F. Sun, M. Lee, E. S. Choi, J. Oitmaa, C. D. Batista, M. Mourigal, H. D. Zhou, and J. Ma, $\text{Ba}_8\text{CoNb}_6\text{O}_{24}$: A spin- $\frac{1}{2}$ triangular-lattice Heisenberg antiferromagnet in the two-dimensional limit, *Phys. Rev. B* **95**, 060412(R) (2017).
- [29] I. P. Muthuselvam, R. Sankar, A. V. Ushakov, G. N. Rao, S. V. Streltsov, and F. C. Chou, Two-step antiferromagnetic transition and moderate triangular frustration in $\text{Li}_2\text{Co}(\text{WO}_4)_2$, *Phys. Rev. B* **90**, 174430 (2014).
- [30] H. Liu and G. Khaliullin, Pseudospin exchange interactions in d^7 cobalt compounds: Possible realization of the Kitaev model, *Phys. Rev. B* **97**, 014407 (2018).
- [31] R. Sano, Y. Kato, and Y. Motome, Kitaev-Heisenberg Hamiltonian for high-spin d^7 Mott insulators, *Phys. Rev. B* **97**, 014408 (2018).
- [32] H. Liu, J. Chaloupka, and G. Khaliullin, Kitaev Spin Liquid in 3d Transition Metal Compounds, *Phys. Rev. Lett.* **125**, 047201 (2020).
- [33] G. Lin, J. Jeong, C. Kim, Y. Wang, Q. Huang, T. Masuda, S. Asai, S. Itoh, G. Günther, M. Russina, Z. Lu, J. Sheng, L. Wang, J. Wang, G. Wang, Q. Ren, C. Xi, W. Tong, L. Ling, Z. Liu *et al.*, Field-induced quantum spin disordered state in spin-1/2 honeycomb magnet $\text{Na}_2\text{Co}_2\text{TeO}_6$, *Nat. Commun.* **12**, 5559 (2021).
- [34] R. Zhong, T. Gao, N. P. Ong, and R. J. Cava, Weak-field induced nonmagnetic state in a Co-based honeycomb, *Sci. Adv.* **6**, eaay6953 (2020).
- [35] M. Lee, E. Choi, J. Ma, R. Sinclair, C. D. Cruz, and H. Zhou, Magnetism and multiferroicity of an isosceles triangular lattice antiferromagnet $\text{Sr}_3\text{NiNb}_2\text{O}_9$, *J. Phys.: Condens. Matter* **28**, 476004 (2016).
- [36] V. Ting, Y. Liu, R. Withers, and L. Norén, An electron diffraction and bond valence sum study of the space group symmetries and structures of the photocatalytic 1:2 B site ordered $\text{A}_3\text{CoNb}_2\text{O}_9$ perovskites ($\text{A}=\text{Ca}^{2+}$, Sr^{2+} , Ba^{2+}), *J. Solid State Chem.* **177**, 2295 (2004).
- [37] D. T. Liu, F. J. Burnell, L. D. C. Jaubert, and J. T. Chalker, Classical spin liquids in stacked triangular-lattice Ising antiferromagnets, *Phys. Rev. B* **94**, 224413 (2016).
- [38] J. Rodríguez-Carvajal, Recent advances in magnetic structure determination by neutron powder diffraction, *Phys. B: Condens. Matter* **192**, 55 (1993).
- [39] A. A. Tsirlin, B. Schmidt, Y. Skourski, R. Nath, C. Geibel, and H. Rosner, Exploring the spin- $\frac{1}{2}$ frustrated square lattice model with high-field magnetization studies, *Phys. Rev. B* **80**, 132407 (2009); Y. Skourski, M. D. Kuz'min, K. P. Skokov, A. V. Andreev, and J. Wosnitza, High-field magnetization of $\text{Ho}_2\text{Fe}_{17}$, *ibid.* **83**, 214420 (2011).
- [40] Y. Haraguchi, T. Ohnoda, A. Matsuo, K. Kindo, and H. A. Katori, Perfect kagome-lattice antiferromagnets with $J_{\text{eff}} = \frac{1}{2}$: The Co^{2+} analogs of the copper minerals volborthite and vesignieite, *Phys. Rev. B* **106**, 214421 (2022); P. Pietrzyk, M. Srebro, M. Radoń, Z. Sojka, and A. Michalak, Spin ground state and magnetic properties of cobalt(II): Relativistic DFT calculations guided by EPR measurements of Bis(2,4-acetylacetonate)cobalt(II)-based complexes, *J. Phys. Chem. A* **115**, 2316 (2011).
- [41] C. Wellm, W. Roscher, J. Zeisner, A. Alfonsov, R. Zhong, R. J. Cava, A. Savoyant, R. Hayn, J. van den Brink, B. Büchner, O. Janson, and V. Kataev, Frustration enhanced by Kitaev exchange in a $\tilde{J}_{\text{eff}} = \frac{1}{2}$ triangular antiferromagnet, *Phys. Rev. B* **104**, L100420 (2021).
- [42] C. Domb and A. Miedema, Chapter VI magnetic transitions, *J. Low Temp. Phys.* **4**, 296 (1964).
- [43] Note that, as the pulse-field magnetization measurements are performed adiabatically at $T = 1.4$ K, there would be an adiabatic temperature change (ΔT_{ad}) with increasing field due to magnetocaloric effect (MCE). At $T = 1.4$ K, we calculated $\Delta T_{\text{ad}} \sim 0.6$ K, which sets an error bar of $T = (1.4 \pm 0.6)$ K. Thus, the scaling of pulse-field data at $T = 1.4$ K with respect to the SQUID data at $T = 1.8$ K is reasonable.
- [44] H. Kawamura and S. Miyashita, Phase transition of the Heisenberg antiferromagnet on the triangular lattice in a magnetic field, *J. Phys. Soc. Jpn.* **54**, 4530 (1985).
- [45] M. V. Gvozdikova, P.-E. Melchy, and M. E. Zhitomirsky, Magnetic phase diagrams of classical triangular and kagome antiferromagnets, *J. Phys.: Condens. Matter* **23**, 164209 (2011).
- [46] L. Seabra, T. Momoi, P. Sindzingre, and N. Shannon, Phase diagram of the classical heisenberg antiferromagnet on a triangular lattice in an applied magnetic field, *Phys. Rev. B* **84**, 214418 (2011).
- [47] D. Yamamoto, C. Suzuki, G. Marmorini, S. Okazaki, and N. Furukawa, Quantum and Thermal Phase Transitions of the Triangular $\text{SU}(3)$ Heisenberg Model under Magnetic Fields, *Phys. Rev. Lett.* **125**, 057204 (2020).
- [48] E. Grivei, V. Bayot, L. Piraux, and J.-P. Issi, Nuclear Schottky effect in thulium, *Phys. Rev. B* **51**, 1301 (1995); K. An, T. Sakakibara, R. Settai, Y. Onuki, M. Hiragi, M. Ichioka, and K. Machida, Sign Reversal of Field-Angle Resolved Heat Capacity Oscillations in a Heavy Fermion Superconductor CeCoIn_5 and $d_{x^2-y^2}$ Pairing Symmetry, *Phys. Rev. Lett.* **104**, 037002 (2010).
- [49] S. J. Sebastian, K. Somesh, M. Nandi, N. Ahmed, P. Bag, M. Baenitz, B. Koo, J. Sichelschmidt, A. A. Tsirlin, Y. Furukawa, and R. Nath, Quasi-one-dimensional magnetism in the spin- $\frac{1}{2}$ antiferromagnet $\text{BaNa}_2\text{Cu}(\text{VO}_4)_2$, *Phys. Rev. B* **103**, 064413 (2021).
- [50] F. Matsubara, Magnetic ordering in a hexagonal antiferromagnet, *J. Phys. Soc. Jpn.* **51**, 2424 (1982).
- [51] S. Miyashita and H. Kawamura, Phase transitions of anisotropic Heisenberg antiferromagnets on the triangular lattice, *J. Phys. Soc. Jpn.* **54**, 3385 (1985).
- [52] G. Quirion, M. Lapointe-Major, M. Poirier, J. A. Quilliam, Z. L. Dun, and H. D. Zhou, Magnetic phase diagram of $\text{Ba}_3\text{CoSb}_2\text{O}_9$ as determined by ultrasound velocity measurements, *Phys. Rev. B* **92**, 014414 (2015).
- [53] K. M. Ranjith, R. Nath, M. Majumder, D. Kasinathan, M. Skoulatos, L. Keller, Y. Skourski, M. Baenitz, and A. A. Tsirlin, Commensurate and incommensurate magnetic order in spin-1 chains stacked on the triangular lattice in $\text{Li}_2\text{NiW}_2\text{O}_8$, *Phys. Rev. B* **94**, 014415 (2016).
- [54] M. E. Lines, Magnetic properties of CoCl_2 and NiCl_2 , *Phys. Rev.* **131**, 546 (1963); H. Shiba, Y. Ueda, K. Okunishi, S. Kimura, and K. Kindo, Exchange interaction via crystal-field excited states and its importance in CsCoCl_3 , *J. Phys. Soc. Jpn.* **72**, 2326 (2003).
- [55] L. Ding, P. Manuel, S. Bachus, F. Grüber, P. Gegenwart, J. Singleton, R. D. Johnson, H. C. Walker, D. T. Adroja, A. D. Hillier, and A. A. Tsirlin, Gapless spin-liquid state in the

- structurally disorder-free triangular antiferromagnet NaYbO₂, *Phys. Rev. B* **100**, 144432 (2019).
- [56] E. S. R. Gopal, *Specific Heats at Low Temperatures* (Springer Science & Business Media, New York, 2012).
- [57] R. Nath, K. M. Ranjith, B. Roy, D. C. Johnston, Y. Furukawa, and A. A. Tsirlin, Magnetic transitions in the spin- $\frac{5}{2}$ frustrated magnet BiMn₂PO₆ and strong lattice softening in BiMn₂PO₆ and BiZn₂PO₆ below 200 K, *Phys. Rev. B* **90**, 024431 (2014).
- [58] Y. Ran, M. Hermele, P. A. Lee, and X.-G. Wen, Projected-Wave-Function Study of the Spin-1/2 Heisenberg Model on the Kagomé Lattice, *Phys. Rev. Lett.* **98**, 117205 (2007).
- [59] M. Hermele, Y. Ran, P. A. Lee, and X.-G. Wen, Properties of an algebraic spin liquid on the kagome lattice, *Phys. Rev. B* **77**, 224413 (2008).
- [60] S. Kundu, A. Shahee, A. Chakraborty, K. M. Ranjith, B. Koo, J. Sichelschmidt, M. T. F. Telling, P. K. Biswas, M. Baenitz, I. Dasgupta, S. Pujari, and A. V. Mahajan, Gapless Quantum Spin Liquid in the Triangular System Sr₃CuSb₂O₉, *Phys. Rev. Lett.* **125**, 267202 (2020).
- [61] S. Nakatsuji, Y. Nambu, H. Tonomura, O. Sakai, S. Jonas, C. Broholm, H. Tsunetsugu, Y. Qiu, and Y. Maeno, Spin disorder on a triangular lattice, *Science* **309**, 1697 (2005).
- [62] J. S. Helton, K. Matan, M. P. Shores, E. A. Nytko, B. M. Bartlett, Y. Yoshida, Y. Takano, A. Suslov, Y. Qiu, J.-H. Chung, D. G. Nocera, and Y. S. Lee, Spin Dynamics of the Spin-1/2 Kagome Lattice Antiferromagnet ZnCu₃(OH)₆Cl₂, *Phys. Rev. Lett.* **98**, 107204 (2007).
- [63] Y. Okamoto, M. Nohara, H. Aruga-Katori, and H. Takagi, Spin-Liquid State in the $S = 1/2$ Hyperkagome Antiferromagnet Na₄Ir₃O₈, *Phys. Rev. Lett.* **99**, 137207 (2007).
- [64] L. Clark, J. C. Orain, F. Bert, M. A. De Vries, F. H. Aidoudi, R. E. Morris, P. Lightfoot, J. S. Lord, M. T. F. Telling, P. Bonville, J. P. Attfield, P. Mendels, and A. Harrison, Gapless Spin Liquid Ground State in the $S=1/2$ Vanadium Oxyfluoride Kagome Antiferromagnet [NH₄]₂[C₇H₁₄N][V₇O₆F₁₈], *Phys. Rev. Lett.* **110**, 207208 (2013).
- [65] J. G. Cheng, G. Li, L. Balicas, J. S. Zhou, J. B. Goodenough, C. Xu, and H. D. Zhou, High-Pressure Sequence of Ba₃NiSb₂O₉ Structural Phases: New $S = 1$ Quantum Spin Liquids Based on Ni²⁺, *Phys. Rev. Lett.* **107**, 197204 (2011).
- [66] H. D. Zhou, E. S. Choi, G. Li, L. Balicas, C. R. Wiebe, Y. Qiu, J. R. D. Copley, and J. S. Gardner, Spin Liquid State in the $S = 1/2$ Triangular Lattice Ba₃CuSb₂O₉, *Phys. Rev. Lett.* **106**, 147204 (2011); O. Mustonen, S. Vasala, E. Sadrollahi, K. P. Schmidt, C. Baines, H. C. Walker, I. Terasaki, F. J. Litterst, E. Baggio-Saitovitch, and M. Karppinen, Spin-liquid-like state in a spin-1/2 square-lattice antiferromagnet perovskite induced by $d^{10} - d^0$ cation mixing, *Nat. Commun.* **9**, 1085 (2018).
- [67] S. Trebst and C. Hickey, Kitaev materials, *Phys. Rep.* **950**, 1 (2022); G. Jackeli and G. Khaliullin, Mott Insulators in the Strong Spin-Orbit Coupling Limit: From Heisenberg to a Quantum Compass and Kitaev Models, *Phys. Rev. Lett.* **102**, 017205 (2009).
- [68] H. Takagi, T. Takayama, G. Jackeli, G. Khaliullin, and S. E. Nagler, Concept and realization of Kitaev quantum spin liquids, *Nat. Rev. Phys.* **1**, 264 (2019).
- [69] S.-H. Baek, S.-H. Do, K.-Y. Choi, Y. S. Kwon, A. U. B. Wolter, S. Nishimoto, J. van den Brink, and B. Büchner, Evidence for a Field-Induced Quantum Spin Liquid in α -RuCl₃, *Phys. Rev. Lett.* **119**, 037201 (2017).
- [70] R. Zhong, M. Chung, T. Kong, L. T. Nguyen, S. Lei, and R. J. Cava, Field-induced spin-liquid-like state in a magnetic honeycomb lattice, *Phys. Rev. B* **98**, 220407(R) (2018).
- [71] M. Ulaga, J. Kokalj, A. Wietek, A. Zorko, and P. Prelovšek, Quantum spin liquid in the easy-axis Heisenberg model on frustrated lattices, [arXiv:2307.03545](https://arxiv.org/abs/2307.03545).
- [72] A. P. Ramirez, Strongly geometrically frustrated magnets, *Annu. Rev. Mater. Sci.* **24**, 453 (1994).
- [73] M. Watanabe, N. Kurita, H. Tanaka, W. Ueno, K. Matsui, T. Goto, and M. Hagihala, Contrasting magnetic structures in SrLaCuSbO₆ and SrLaCuNbO₆: Spin- $\frac{1}{2}$ quasi-square-lattice $J_1 - J_2$ Heisenberg antiferromagnets, *Phys. Rev. B* **105**, 054414 (2022).
- [74] I. Nishizawa, N. Kurita, H. Tanaka, and T. Goto, Magnetic phase diagram in the three-dimensional triangular-lattice antiferromagnet Sr₃CoTa₂O₉ with small easy-axis anisotropy, *Phys. Rev. B* **107**, 174419 (2023).